Journal of Nuclear Materials 392 (2009) 6–15

Contents lists available at ScienceDirect

Journal of Nuclear Materials

journal homepage: www.elsevier.com/locate/jnucmat

Three dimensional coupled simulation of thermomechanics, heat, and oxygen diffusion in UO_2 nuclear fuel rods

Chris Newman, Glen Hansen *, Derek Gaston

Multiphysics Methods Group, Idaho National Laboratory, P.O. Box 1625, Idaho Falls, ID 83415-3840, United States

ARTICLE INFO

Article history:
Received 24 November 2008
Accepted 2 March 2009

ABSTRACT

The simulation of nuclear reactor fuel performance involves complex thermomechanical processes between fuel pellets, made of fissile material, and the protective cladding barrier that surrounds the pellets. This paper examines a subset of phenomena that are important in the development of an analysis capability for fuel performance calculations, focusing on thermomechanics and diffusion within UO_2 fuel pellets. In this study, correlations from the literature are used for thermal conductivity, specific heat, and oxygen diffusion. This study develops a three dimensional thermomechanical model fully-coupled to an oxygen diffusion model. Both steady state and transient results are examined to compare this three dimensional model with the literature. Further, this equation system is solved in a parallel, fully-coupled, fully-implicit manner using a preconditioned Jacobian-free Newton Krylov method. Numerical results are presented to explore the efficacy of this approach for examining selected fuel performance problems. INL's `BISON` fuels performance code is used to perform this analysis.

1. Introduction

Economical operation is an important design and operational objective for oxide fuel for use in light water reactors. As an oversimplification, economical operation results when the life of a fuel rod can be maximized (in terms of burnup) without resulting in fuel failure or maintenance issues when replacing fuel rods. Numerical modeling of fuel materials (in this case UO_2 pellets) will be an essential tool in support of this objective by providing a relatively inexpensive mechanism for studying the impact of design and operational changes on the life of a fuel rod.

Fuel failure may be traced to several phenomena, including corrosion, mechanical (fretting) wear, and pellet cladding interaction [1]. The recent Fuel Modeling at Extended Burnup (FUMEX II) report [2] discusses several limitations of current fuel modeling capabilities. This report concludes with 'Mechanical interaction is not well developed and further work in this area would be useful.' Limiting this discussion to pellet cladding interaction (PCI), many processes affect the nature of pellet expansion, the characteristics of that expansion, and the geometry of pellet cladding contact; namely the thermomechanics of the pellet and all processes that govern pellet dynamics.

Ramirez et al. [3] present a numerical study of coupled heat and oxygen diffusion in UO_2 fuel pellets. The steady state results in [3] have since been repeated by Shadid and Hooper within the `PelletTransport` example in Trilinos [4]. The Ramirez study employed a one dimensional simulation to examine both the transient and steady state relationship between temperature and oxygen nonstoichiometry. The article concludes that hyperstoichiometry significantly impacts the thermal conductivity of UO_2 which affects the maximum temperature of the fuel rod. Transient calculations confirm a significant separation of time scales between the thermal heating of a pellet and the hyperstoichiometric profile within the pellet. One path toward an analysis capability for PCI might involve extending [3,4] to three dimensions, adding mechanics models for the pellet and cladding and a contact model to transfer stresses to the cladding from the pellet, and add the remaining physics that impact cladding integrity. Indeed, this paper proposes an intermediate result needed to achieve that objective.

This report examines a subset of processes that influence PCI; the thermomechanics of a thermally-expanding pellet where the expansion is a function of the local oxygen-to-metal (O/M) ratio of the fuel. It proposes a three dimensional linear elastic finite element model for the displacement of the pellet, and couples this displacement to a three dimensional heat equation. These two equations are coupled to a third, three dimensional oxygen diffusion equation. While the displacement equation is linear, the composite problem is nonlinear as the governing equations are coupled together by material properties that are generally functions of density (modified by displacement), hyperstoichiometry (modified by temperature), temperature (modified by thermal conductivity that is a function of hyperstoichiometry), etc. The use of operator split methods for the solution of coupled multiphysics problems of this sort can lead to both stability and accuracy issues [5–7]. To avoid

* Corresponding author.
E-mail addresses: Christopher.Newman@inl.gov (C. Newman), Glen.Hansen@inl.gov (G. Hansen), Derek.Gaston@inl.gov (D. Gaston).

0022-3115/$ - see front matter © 2009 Elsevier B.V. All rights reserved.
doi:10.1016/j.jnucmat.2009.03.035

these considerations here, the composite nonlinear algebraic system resulting from the finite element discretization of the equations is solved in a fully-coupled manner using a preconditioned Jacobian-free Newton Krylov (JFNK) [8] method.

Ramirez shows that the thermal and oxygen diffusion problems operate on significantly different time scales, related to the Lewis number $L_e = \kappa/D$, where κ is the thermal diffusivity of the UO_2 pellet and D is the chemical diffusivity of oxygen in the pellet. In a realistic PCI calculation, there will be as a minimum two additional time scales to be considered; one due to fission product driven mechanical swelling of the pellet and a second that accounts for the thermal and mechanical interaction between the pellet and cladding across the narrowing gap. These disparate time scales are expected to combine with the pellet (and cladding) mechanics models and the contact model across the gap to result in a very challenging numerical problem to solve. These considerations further support the choice of the fully-implicit JFNK approach outlined in this paper as there are many examples in the literature that propose the use of such a method on stiff coupled problems with disparate length and time scales [9–11]. To our knowledge, this paper details the first application of the parallel JFNK method to the aforementioned reactor fuels application.

Higgs et al. [12] develop a two dimensional $(r-z)$ multiphysics model for fuel oxidation of defective fuel. This is a sophisticated model, considering

1. gas phase transport in the pellet cladding gap,
2. interstitial oxygen diffusion in the pellet matrix,
3. gas phase transport in the fuel cracks, and
4. heat conduction in the pellet.

The present study considers only items 2 and 4 of Higg's model (a boundary condition is used that partially addresses 1), but notes that the remainder of these capabilities will be important for a fuel performance simulation capability. The degree of complexity of such a simulation capability will require the development of effective preconditioning approaches for the JFNK method. This study begins that development by examining preconditioning for the coupled thermomechanics and oxygen diffusion equations.

Idaho National Laboratory's BISON fuel performance code was used to develop the results shown here. BISON is built upon INL's MOOSE: a parallel, nonlinear, computational framework [13]. MOOSE supports the use of complex, three dimensional meshes and parallel computing that will be necessary for full rod and fuel assembly calculations. This report closes with a demonstration calculation of a dished pellet with a simple crack to illustrate the parallel three dimensional capabilities of the code.

2. Conceptual model

BISON, the fuels performance code developed using the Multiphysics Object Oriented Simulation Environment (MOOSE), is designed for fully-coupled steady and transient analysis and to be efficient on both desktop computers and in massively parallel environments. It employs physics based preconditioned Jacobian-free Newton Krylov solution methods and is developed using modern software engineering principles to form a robust, extensible software architecture to ultimately provide a design and analysis capability for a wide range of nuclear phenomena [13]. This discussion summarizes the current status of the BISON fuel performance analysis code and demonstrates results on selected three dimensional capabilities that support fuel performance calculations.

In a multidimensional simulation, it is not straightforward to maintain a computational mesh in the gap between the pellet and cladding, as illustrated in Fig. 1, due to the composite radial and axial displacement of the outside surface of the pellet with respect to the cladding. The model developed here includes a thermal boundary condition to account for the heat flux from the outside of the pellet, through the gap and cladding, to the coolant (c.f., Fig. 2). Further, the pellet is free to expand without being checked by the cladding. Future work entails a more realistic gap and cladding model; however, the approach presented here is sufficient to allow comparison with the results in [3]. The problem consists of three fully-coupled partial differential equations for heat conduction, oxygen nonstoichiometry and linear elastic solid mechanics. Let $\Omega \in \mathbb{R}^d$, $d = 2, 3$ define the computational domain (the fuel pellet).

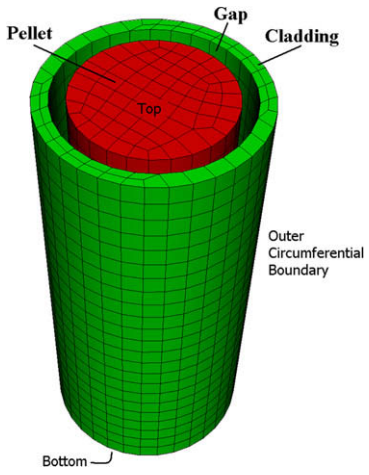

Fig. 1. Pictorial of the conceptual model.

2.1. Pellet heat conduction model

The heat conduction model assumes fission reactions generate heat at a uniformly distributed constant rate, Q,

$$\begin{aligned} &\rho C_p \frac{\partial T}{\partial t} + \nabla \cdot \mathbf{q} - Q = 0 \quad T \in \Omega, \\ &\mathbf{n} \cdot \mathbf{q} = q(T) \quad T \in \Gamma^C, \\ &\mathbf{n} \cdot \mathbf{q} = 0 \quad T \in \Gamma^T \cup \Gamma^B, \\ &T(t=0) = T_0 \quad T \in \Omega, \end{aligned} \tag{1}$$

where T, ρ and C_p are temperature, density and specific heat of UO_2, respectively. The empirical models for these quantities are given in Table 1, and match the values used in [3]. Here, Γ^T denotes the top and Γ^B denotes the bottom boundary of the fuel pellet, and Γ^C denotes the outer circumferential fuel pellet boundary such that $\Gamma = \Gamma^T \cup \Gamma^B \cup \Gamma^C$, and $q(T)$ is given by a clad and gap heat conductance model,

$$q(T) = \frac{T_p - T_w}{\frac{L_g}{k(\mathrm{He})} + \frac{L_c}{k(\mathrm{clad})}}, \tag{2}$$

where the values for k are given in Tables 2 and 3, the temperatures T_p, T_w and lengths L_g and L_c are shown in Fig. 2, and the geometric configuration is illustrated in Fig. 1. The heat flux $\mathbf{q}$ within the UO_2 domain Ω may be written as [14]

$$\mathbf{q} = -k\nabla T - Q^* D \nabla C, \tag{3}$$

where k, D, and Q^* denote thermal conductivity, heat of transport of oxygen, and ∇C is the concentration gradient, respectively (c.f., Table 1). For the configuration studied, both the concentration gradient and D are small, as is the actual transfer of mass due to oxygen diffusion. The last term is therefore much smaller than $k\nabla T$, thus it is neglected in this study, as it was in [3].

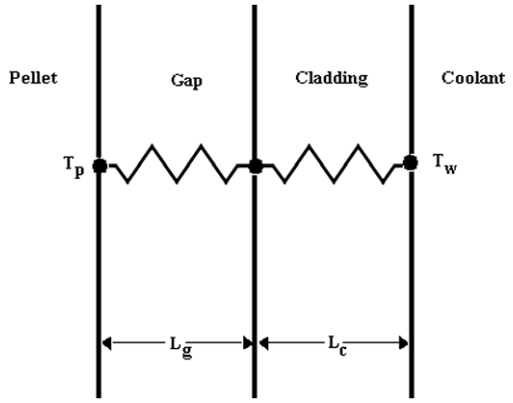

Fig. 2. Pictorial of the pellet, gap, clad geometry used for the thermal boundary condition on the outside of the pellet in (2).

2.2. Oxygen diffusion model

A hyperstoichiometric model for oxygen is given in [3]. Let **J** denote the oxygen flux in the hyperstoichiometric regime with,

$$\mathbf{J} = -D\left(\nabla x - \frac{xQ^*}{FRT^2}\nabla T\right), \tag{4}$$

Table 2
Material properties for He.

Property	Value	Units	Source
ρ(He)	$\rho(T) = 0.0818 - 8275 \times 10^{-5}(T - 600.0)$	kg m^{-3}	[3]
C_p(He)	$C_p = 5190.0$	J kg^{-1} K^{-1}	[3]
k(He)	$0.0468 + 3.81 \times 10^{-4}T - 6.79 \times 10^{-8}T^2$	W m^{-1} K^{-1}	[3]

where D is diffusivity of UO_2, F is the thermodynamic factor of oxygen, Q^* is the heat of transport of oxygen, and R is the universal gas constant. The empirical models for these properties are given in Table 1. The nonstoichiometric model for oxygen diffusion, x, is given by

$$\begin{aligned} &\frac{\partial x}{\partial t} + \nabla \cdot \mathbf{J} = 0 \quad x \in \Omega, \\ &\mathbf{n} \cdot \mathbf{J} = 0 \quad x \in \Gamma^T \cup \Gamma^B, \\ &x = x_d \quad x \in \Gamma^C, \\ &x(t=0) = x_0 \quad x \in \Omega. \end{aligned} \tag{5}$$

2.3. Solid mechanics model

Simulations performed by Ramirez et al. [3] indicate a temperature difference of ~ 350 K from the center of the fuel pellet to the

Table 1
Material properties for UO_2.

Property	Value	Units	Source
$\rho(UO_2)$	$\rho(T) = 10960(a + bT + cT^2 + dT^3)^{-3}$	kg m^{-3}	[18][a]
	$a = 0.997$, $b = 9.802 \times 10^{-6}$, $c = -2.705 \times 10^{-10}$, $d = 4.391 \times 10^{-13}$ for $T < 923$ K		
	$a = 0.997$, $b = 1.179 \times 10^{-5}$, $c = -2.429 \times 10^{-9}$, $d = 1.219 \times 10^{-12}$ for $T > 923$ K		
$C_p(UO_2)$	$C_p(T) = 264.256 + 0.047T$	J kg^{-1} K^{-1}	[3][b]
$k(UO_2)$	$k(T,x) = \lambda_0(T)\frac{\arctan(\theta(T,x))}{\theta(T,x)} + 5.95 \times 10^{-11}T^3$	W m^{-1} K^{-1}	[3]
	$\lambda_0(T) = (3.24 \times 10^{-2} + 2.51 \times 10^{-4}T)^{-1}$		
	$\theta(T,x) = 3.67\ \exp(-4.73 \times 10^{-4}T)\sqrt{2x\lambda_0(T)}$		
$\alpha(UO_2)$	$\alpha(T) = a + bT + cT^2 + dT^3$	K^{-1}	[16]
	$a = 9.828 \times 10^{-6}$, $b = -6.390 \times 10^{-10}$, $c = 1.330 \times 10^{-12}$, $d = -1.757 \times 10^{-17}$ for $T < 923$ K		
	$a = 1.1833 \times 10^{-5}$, $b = -5.013 \times 10^{-9}$, $c = 3.756 \times 10^{-12}$, $d = -6.125 \times 10^{-17}$ for $T > 923$ K		
$D_1(UO_2)$	$\log_{10}(D(T,x)) = -9.386 - 4.26 \times 10^3/T + 1.2 \times 10^{-3}Tx + 7.5 \times 10^{-4}T\log_{10}(\frac{2.0+x}{x})$	m^2 s^{-1}	[3]
$D_2(UO_2)$	$\log_{10}(D(x)) = -7.9 + 6x + \log_{10}(2.0 + x) - \log_{10}(x) \quad T = 1273$ K	cm^2 s^{-1}	[19]
$D_3(UO_2)$	$D(T) = 2.5\exp(-16400/T)$	cm^2 s^{-1}	[12]
$Q^*(UO_2)$	$Q^*(x) = -1380.8 - 134435.5\ \exp(-x/0.0261)$	J mol^{-1}	[3]
$F(UO_2)$	$F(x) = \frac{2+x}{2(1-3x)(1-2x)}$	–	[3]
$E(UO_2)$	$E(T,x) = 2.0128416 \times 10^{11}(1.0 - 1.0915 \times 10^{-4}T)\ \exp(-1.75x)$	Pa	[20]
$\nu(UO_2)$	.3	–	[14]

[a] One of the reviewers of this paper noted that the value for $b = 9.082 \times 10^{-6}$ for $T < 923$ K given in [18] is incorrect; this value should be $b = 9.802 \times 10^{-6}$.
[b] The units given in the reference do not appear to be consistent with the magnitude obtained from the correlation presented therein. The authors assume here that the units in the reference should be listed as mJ kg^{-1} K^{-1}, not J kg^{-1} K^{-1}.

Table 3
Material properties for clad.

Property	Value	Units	Source
ρ(clad)	$\rho = 17817.0$	kg m^{-3}	[3]
C_p(clad)	$C_p = 420.0$	J kg^{-1} K^{-1}	[3]
k(clad)	$k(T) = 10.98 + 1.4\times10^{-2}T - 7.44\times10^{-6}T^2$	W m^{-1} K^{-1}	[3]
α(clad)	$\alpha(T) = 1\times10^{-6}(16.0 + 4.62\times10^{-3}T)$	K^{-1}	[14]
E(clad)	$E(T) = 9.21\times10^{10} - 4.05\times10^{7}T$	Pa	[20]
ν(clad)	.32	–	[14]

outer edge, where the center of the pellet is at ~ 1150 K. At these temperatures, Olander [14] describes polycrystalline UO_2 as a brittle material. Recent models treat the pellet as an incompressible viscoelastic material and also take in account irradiation, porosity, and thermal creep [15]. For simplicity, this paper considers the pellet as a uniform, pure elastic material, and leaves more realistic mechanics to future work.

This study does not include the effect of porosity, but it does include the effect of temperature and hyperstoichiometry on Young's modulus (c.f., Table 1). Poisson's ratio is assumed to remain constant at a value of 0.3, although a better result could be obtained by considering porosity and the increase of Poisson's ratio with temperature [14]. A temperature-dependent thermal expansion coefficient α is employed in the thermal expansion term. Neither thermal expansion or density of UO_2 are adjusted for departure from stoichiometry as they appear to be insensitive to this effect [16,17].

The pellet is assumed to be fracture and defect free initially, and it remains so throughout the simulation, even though thermally driven stresses occur that are significantly beyond the fracture stress of the oxide. Further, this study assumes that as the outside surface of the pellet expands thermally, the cladding translates outward at the same rate such that the gap distance remains constant and the pellet and cladding do not interact mechanically. Lastly, the study does not consider any radiation effects, change in material properties due to burnup, or the formation of fission products or swelling of the pellet due to fission product accumulation.

Clearly, this is a very limited mechanics model, useful only for development and prototyping activities. Future work includes development of a fully-coupled pellet cladding mechanical interaction (PCMI) capability, more sophisticated material closure models, fracture capabilities, and fission product driven swelling of the pellet. Additionally, a nonlinear mechanical model for the cladding must be added that includes plasticity, history dependent radiation hardening, void swelling, radiation induced creep, and corrosion effects.

A linear elastic model for the displacement $\mathbf{u}$, using the closure relationships in Table 1, was employed in this study as

$$\begin{aligned}
&\frac{\partial^2\mathbf{u}}{\partial t^2} - \mathrm{A}^{\mathrm{T}}\mathrm{DA}\mathbf{u} + f = 0 \quad \mathbf{u}\in\Omega,\\
&\mathbf{u} = 0 \quad \mathbf{u}\in\Gamma^B,\\
&\mathbf{u}(t=0) = \mathbf{u}_0 \quad \mathbf{u}\in\Omega,\\
&\frac{\partial\mathbf{u}}{\partial t}(t=0) = \mathbf{u}_{00} \quad \mathbf{u}\in\Omega,
\end{aligned} \tag{6}$$

with

$$\mathrm{A} = \begin{bmatrix} \partial_x & 0 & 0\\ 0 & \partial_y & 0\\ 0 & 0 & \partial_z\\ \partial_y & \partial_x & 0\\ 0 & \partial_z & \partial_y\\ \partial_z & 0 & \partial_x \end{bmatrix}, \quad \mathrm{D} = c_1\begin{bmatrix} 1 & c_2 & c_2 & 0 & 0 & 0\\ c_2 & 1 & c_2 & 0 & 0 & 0\\ c_2 & c_2 & 1 & 0 & 0 & 0\\ 0 & 0 & 0 & c_3 & 0 & 0\\ 0 & 0 & 0 & 0 & c_3 & 0\\ 0 & 0 & 0 & 0 & 0 & c_3 \end{bmatrix},$$

and

$$c_1 = \frac{E(1-\nu)}{(1+\nu)(1-\nu)}, \quad c_2 = \frac{\nu}{(1-\nu)}, \quad c_3 = \frac{(1-2\nu)}{2(1-\nu)}.$$

The coefficients E and ν are Young's modulus and Poisson's ratio. They are summarized in Table 1 for the pellet. Eq. (6) is not valid nor applied in the gap or cladding. The forcing term f weakly enforces linear thermal expansion with coefficient α. The thermal expansion coefficient α is given in Table 1 for the pellet.

2.4. Material property models

Material properties employed in this study for UO_2, the helium within the gap (He), and the cladding material are described in Tables 1–3. These models were compiled from multiple sources (listed in the fourth column).

2.5. Finite element discretization

Given the domain $\Omega\in\mathbb{R}^3$, the coordinate system of interest is written as $\mathbf{x} = (x_1, x_2, x_3)$. The solution to the coupled Eqs. (1)–(6) is approximated with a semidiscrete method consisting of a finite element discretization of space and a finite difference discretization of time. To develop weak forms for (1)–(6), one seeks approximate values of T, $x\in V$, and $\mathbf{u}\in W = V\times V\times V$, where V is an appropriate subspace of $H^1(\Omega)$, such that

$$\left(\rho C_p T_t - Q, v\right) + \left(k\nabla T, \nabla v\right) - \langle q(T), v\rangle_{\Gamma_c} = 0, \tag{7}$$

$$(x_t, v) + \left(D\left(\nabla x + \frac{xQ^*}{FRT^2}\nabla T\right), \nabla v\right) = 0, \tag{8}$$

and

$$(\mathbf{u}_{tt}, \mathbf{w}) + \mu S(\mathbf{u}, \mathbf{w}) + \lambda(\nabla\cdot\mathbf{u}, \nabla\cdot\mathbf{w}) - ((T - T_{\mathrm{ref}})\mathbf{a}, \nabla\mathbf{w}) = 0, \tag{9}$$

for all $v\in V$ and $\mathbf{w}\in W$. In (7)–(9), $(\cdot,\cdot)$ denotes the inner product in $L^2(\Omega)$, $\langle\cdot,\cdot\rangle_\Gamma$ is the inner product in $L^2(\Gamma)$, the subscript t in $(\cdot)_t$ denotes the partial of $(\cdot)$ with respect to time, $\mathbf{a} = \alpha[1,1,1]^{\mathrm{T}}$, and

$$S(\mathbf{u}, \mathbf{w}) = \sum_{i,j=1}^{3}\left(\partial_j u_i + \partial_i u_j\right)\left(\partial_j w_i + \partial_i w_j\right), \tag{10}$$

where $\mu = \frac{E}{2(1-\nu)}$ and $\lambda = \frac{E\nu}{(1+\nu)(1-2\nu)}$. In (9), T_{ref} is the temperature corresponding to zero displacement of the pellet, in this case 273 K.

The test space V is approximated by V^h using linear Lagrange finite elements such that $V^h\subset V$ and $V^h = \mathrm{span}\{\phi_i\}_{i=1}^n$. Then

$$\left(\rho C_p T_t - Q, \phi_i\right) + \left(k\nabla T, \nabla\phi_i\right) - \langle q(T), \phi_i\rangle_{\Gamma_c} = 0, \tag{11}$$

$$(x_t, \phi_i) + \left(D\left(\nabla x + \frac{xQ^*}{FRT^2}\nabla T\right), \nabla\phi_i\right) = 0, \tag{12}$$

and

$$(\mathbf{u}_{tt}, \Phi_i) + \mu S(\mathbf{u}, \Phi_i) + \lambda(\nabla\cdot\mathbf{u}, \nabla\cdot\Phi_i) - ((T - T_{\mathrm{ref}})\mathbf{a}, \nabla\Phi_i) = 0, \tag{13}$$

where $\Phi_i = \phi_i[1,1,1]^{\mathrm{T}}$ holds for all ϕ_i. The trial space in (11)–(13) is approximated similarly, where each $v\in V^h$ may be expressed as $v(t,\mathbf{x}) = \sum_{j=1}^n v_j(t)\phi_j(\mathbf{x})$. Thus (11)–(13) can be written as

$$\sum_{j=1}^{n}\left(\rho C_p(T_j)_t\phi_j - Q, \phi_i\right) + \left(T_j k\nabla\phi_j, \nabla\phi_i\right) - \langle q(T), \phi_i\rangle_{\Gamma_c} = 0, \tag{14}$$

$$\sum_{j=1}^{n}\left((x_j)_t\phi_j, \phi_i\right) + \left(D\left(x_j\nabla\phi_j + \frac{x_j\phi_j Q^*}{FRT^2}\nabla T\right), \nabla\phi_i\right) = 0, \tag{15}$$

and

$$\sum_{j=1}^{n}\left((\mathbf{u}_j)_{tt}\Phi_j,\Phi_i\right)+\mu\mathbf{u}_jS(\Phi_j,\Phi_i)+\lambda(\nabla\cdot\mathbf{u}_j\Phi_j,\nabla\cdot\Phi_i)-((T-T_{\text{ref}})\mathbf{a},\nabla\Phi_i)=0. \tag{16}$$

Note that (14)–(16) are in the form of a vector of nonlinear equations $\mathbf{F}(\mathbf{x})=0$, with

$$\mathbf{F}^1(\mathbf{T})=\sum_{j=1}^{n}\left(\rho C_p(T_j)_t\phi_j-Q,\phi_i\right)+\left(T_jk\nabla\phi_j,\nabla\phi_i\right)-\langle q(T),\phi_i\rangle_{\Gamma_c}, \tag{17}$$

$$\mathbf{F}^2(\mathbf{x})=\sum_{j=1}^{n}\left((x_j)_t\phi_j,\phi_i\right)+\left(D\left(x_j\nabla\phi_j+\frac{x_j\phi_jQ^*}{FRT^2}\nabla T\right),\nabla\phi_i\right), \tag{18}$$

and

$$\mathbf{F}^3(\mathbf{u})=\sum_{j=1}^{n}\left((\mathbf{u}_j)_{tt}\Phi_j,\Phi_i\right)+\mu\mathbf{u}_jS(\Phi_j,\Phi_i)+\lambda(\nabla\cdot\mathbf{u}_j\Phi_j,\nabla\cdot\Phi_i)-((T-T_{\text{ref}})\mathbf{a},\nabla\Phi_i), \tag{19}$$

where $\mathbf{T}$, $\mathbf{x}$ and $\mathbf{u}$ are vectors of unknowns with $(\mathbf{T})_i=T_i$, $(\mathbf{x})_i=x_i$ and $(\mathbf{u})_i=\mathbf{u}_i$.

2.6. Time integration

Eqs. (17)–(19) are integrated in time using the implicit Euler method [21]. Let T^k, x^k and $\mathbf{u}^k$ denote T, x and $\mathbf{u}$ at time step k. Then (17) and (18) are discretized in time as

$$\mathbf{F}^1(\mathbf{T})=\sum_{j=1}^{n}\frac{\rho C_p\left(T_j^{k+1}-T_j^k\right)}{\Delta t}(\phi_j,\phi_i)-(Q,\phi_i)+\left(T_j^{k+1}k\nabla\phi_j,\nabla\phi_i\right)-\langle q(T^{k+1}),\phi_i\rangle_{\Gamma_c}, \tag{20}$$

$$\mathbf{F}^2(\mathbf{x})=\sum_{j=1}^{n}\frac{\left(x_j^{k+1}-x_j^k\right)}{\Delta t}(\phi_j,\phi_i)+\left(D\left(x_j^{k+1}\nabla\phi_j+\frac{x_j^{k+1}\phi_jQ^*}{FR(T^{k+1})^2}\nabla T^{k+1}\right),\nabla\phi_i\right), \tag{21}$$

and (19) becomes

$$\mathbf{F}^3(\mathbf{u})=\sum_{j=1}^{n}\frac{\left(\mathbf{u}_j^{k+1}-2\mathbf{u}_j^k+\mathbf{u}_j^{k-1}\right)}{\Delta t^2}(\Phi_j,\Phi_i)+\mu\mathbf{u}_j^{k+1}S(\Phi_j,\Phi_i)+\lambda\mathbf{u}_j^{k+1}(\nabla\cdot\Phi_j,\nabla\cdot\Phi_i)-\left((T^{k+1}-T_{\text{ref}})\mathbf{a},\nabla\Phi_i\right). \tag{22}$$

Following relative scaling, the resulting system of nonlinear algebraic equations is solved using the Jacobian-free Newton Krylov nonlinear solver described in Section 2.7.

2.7. The nonlinear solver: Jacobian-free Newton Krylov

The code framework used in this study [13] is designed to support implementation of complex coupled multiphysics equation systems using a preconditioned Jacobian-free Newton Krylov architecture [8]. To summarize this approach in terms of the development of a fuels performance capability:

1. Finite element expressions for the thermomechanics and oxygen diffusion form a nonlinear residual,
2. Newton's method is used to solve for a new problem state,
3. The Jacobian-free approximation is used to eliminate the need to form and store the Jacobian needed by Newton's method.

The Jacobian-free approximation also naturally supports effective coupling between physics and lends itself to an extensible and modular implementation in software. This report presents an efficient iterative solver for the nonlinear system given in (20)–(22) that is based on the Jacobian-free Newton Krylov (JFNK) methodology (c.f. [8] and references contained therein). The JFNK solution method used in BISON begins with writing a weak form of the above system of equations and casting it into a residual function,

$$\mathbf{F}(\mathbf{x})=\mathbf{0}, \tag{23}$$

that is of length N, where N is the number of unknowns in the discrete problem. The Jacobian of this system is an $N\times N$ sparse matrix,

$$\mathscr{J}(\mathbf{x})=\frac{\partial\mathbf{F}(\mathbf{x})}{\partial\mathbf{x}}, \tag{24}$$

where the components of $\mathbf{F}(\mathbf{x})$ are taken directly from Eqs. (20)–(22). Given the Jacobian in this form, it is straightforward to express the Newton iteration,

$$\mathscr{J}(\mathbf{x}^{(k)})\ \delta\mathbf{x}^{(k)}=-\mathbf{F}(\mathbf{x}^{(k)}), \tag{25}$$

and

$$\mathbf{x}^{(k+1)}\leftarrow\ \mathbf{x}^{(k)}+\delta\mathbf{x}^{(k)}, \tag{26}$$

where the superscript k denotes the iteration count of the current Newton iteration. Using Newton's method as shown here amounts to implementing a sequence of steps:

1. Form the Jacobian matrix,
2. Solve the sparse linear system (25) to obtain $\delta\mathbf{x}^{(k)}$,
3. Apply the update (26) to obtain the next iteration of the solution state vector, $\mathbf{x}^{(k+1)}$.

Even for moderately large grids, the cost of forming the Jacobian is high and typically dominates the computation, making the above algorithm impractical for most situations. Fortunately, Krylov iterative solvers such as the generalized minimum residual (GMRES) algorithm [22], which is used here to solve the Jacobian system, do not require the Jacobian matrix itself but simply the action of the Jacobian matrix on a vector. Approximating this matrix vector product by differencing, which requires two nonlinear function evaluations, is the basis of the JFNK method. Specifically, to evaluate the matrix vector product $\mathscr{J}(\mathbf{x}^{(k)})\mathbf{v}$, a finite difference approach,

$$\mathscr{J}(\mathbf{x}^{(k)})\mathbf{v}\approx\frac{\mathbf{F}(\mathbf{x}^{(k)}+\varepsilon\mathbf{v})-\mathbf{F}(\mathbf{x}^{(k)})}{\varepsilon}, \tag{27}$$

is commonly used [8,23]. Here, ε is chosen in an automatic fashion to avoid problems with machine precision,

$$\varepsilon=\frac{\sqrt{(1+\|\mathbf{u}\|_2)\hat{\varepsilon}}}{\|\mathbf{v}\|_2}, \tag{28}$$

with $\hat{\varepsilon}=10^{-12}$.

Using this Jacobian-free approach, the dominant cost of the algorithm shifts from evaluating the Jacobian to the solution of the linear system. Indeed, the solution cost of GMRES for elliptic problems scales quadratically with the number of unknowns in the grid, unless effective preconditioning is used [24]. This work employs physics-based preconditioning where preconditioning is applied to the diagonal blocks of the Jacobian [24,25].

2.8. Preconditioning

In order to efficiently solve (20)–(22) with a Jacobian-free Newton Krylov method, a physics based approach where preconditioning is applied to the elliptic blocks of the Jacobian, is employed. The right preconditioned form of the linear system (25) is

$$\mathscr{J}(\mathbf{x}^{(k)})\, M^{-1}(M\delta\mathbf{x}^{(k)}) = -\mathbf{F}(\mathbf{x}^{(k)}), \tag{29}$$

where M^{-1} symbolically represents the preconditioning process. The matrix free version of (27) is then

$$\mathscr{J}(\mathbf{x}^{(k)})M^{-1}\mathbf{v} \approx \frac{\mathbf{F}(\mathbf{x}^{(k)} + \varepsilon M^{-1}\mathbf{v}) - \mathbf{F}(\mathbf{x}^{(k)})}{\varepsilon}, \tag{30}$$

where $M = \mathrm{diag}(M_1, M_2, M_3)$, with

$$(M_1)_{ij} = \frac{\rho C_p}{\Delta t}(\phi_i, \phi_j) + k(\nabla\phi_i, \nabla\phi_j),$$
$$(M_2)_{ij} = \frac{1}{\Delta t}(\phi_i, \phi_j) + \left(D\left(\nabla\phi_i + \frac{\phi_j Q^*}{FRT^2}\nabla T\right), \nabla\phi_j\right),$$

and

$$(M_3)_{ij} = \frac{1}{\Delta t^2}(\Phi_i, \Phi_j) + \mu S(\Phi_i, \Phi_j) + \lambda(\nabla\cdot\Phi_i, \nabla\cdot\Phi_j).$$

The preconditioner M^{-1} is approximated using the algebraic multigrid package *BoomerAMG* [26] in *Hypre* [27]. Further, *BoomerAMG* may be used in concert with the additive Schwarz method in PETSc [28]. The JFNK iteration is provided by the *SNES* nonlinear solver, also contained in PETSc.

3. Results

With the theoretical and numerical basis of the coupled thermomechanics/oxygen diffusion problem fully developed, this study now examines both steady state and transient problems similar to those considered in [3]. Fig. 3(a) is a geometric representation showing the dimensions of the pellet-gap-cladding system examined in this study. A three dimensional all-hexahedra mesh, generated using CUBIT [29], is used to discretize the pellet (c.f., Fig. 3(b)). Neither the gap between the pellet and cladding or the cladding are meshed; this study assumes that the cladding and pellet do not contact during pellet expansion. Given an appropriate selection of boundary conditions and a uniform gap around the pellet, the results will be axisymmetric. As such, these results may be compared and contrasted with [3].

3.1. Steady state results

The simulation of steady and transient heat and oxygen diffusion in oxide fuels consists of strongly coupled nonlinear heat transfer and diffusion of chemical species within multiple materials including the fuel rod, cladding and gap. Solutions are characterized by strong temperature gradients and for transient simulations; thermal diffusion and diffusion of chemical species that operate on vastly different time scales. The separation of these time scales is quantified by the Lewis number *Le*. To provide the steady state solution to compare with Figs. 2 and 3 of [3], the coupled thermomechanics/oxygen diffusion equation system (1)–(6) was solved, employing fixed Dirichlet conditions of $x = 0.02$ for hyperstoichiometry and $T = 810$ K for temperature on the outside of the pellet and a constant heat source of 2×10^8 W m^{-3}. These results are shown in Figs. 3(b) and 4. The impact of coupled oxygen diffusion is clear on both the pellet temperature and thermal expansion.

Fig. 4 shows the pellet temperature and displacement vs. distance from the center of the pellet. Given the choice of boundary conditions and a constant gap, there is negligible variation of the three dimensional solution for temperature and oxygen nonstoichiometry azimuthally at the center of the pellet, allowing a straightforward comparison with the one dimensional results of Ramirez et al. [3]. The temperature and nonstoichiometry (x) results obtained here are indeed similar. Fig. 4(b) shows the impact of the coupled oxygen diffusion model on pellet displacement.

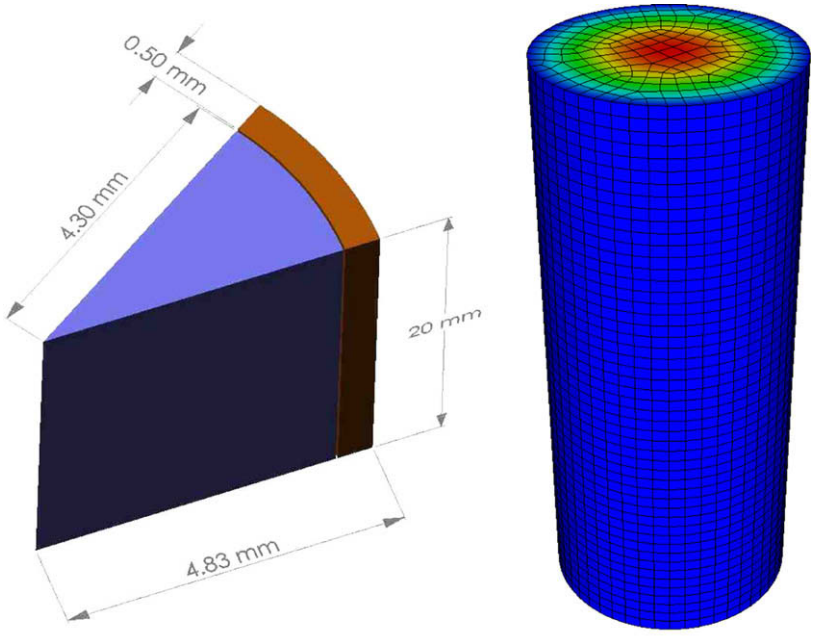

(a) Model dimensions. (b) Three dimensional mesh.

Fig. 3. Pictorial and dimensions of the fuel configuration that is the basis for this study. Mesh is colored with the temperature solution of the steady state problem described in the text. This mesh was used for the following steady state and transient results.

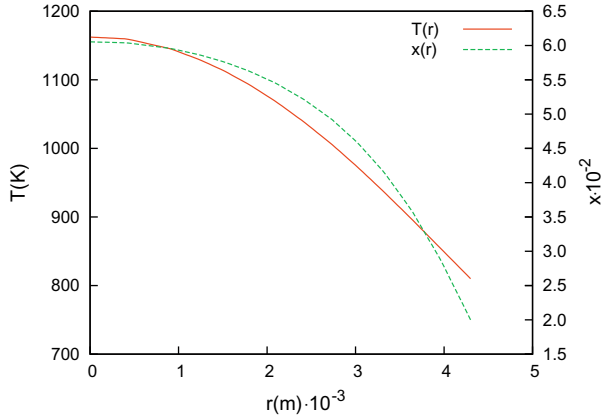

(a) Pellet temperature and oxygen hyperstoichiometry vs. radius.

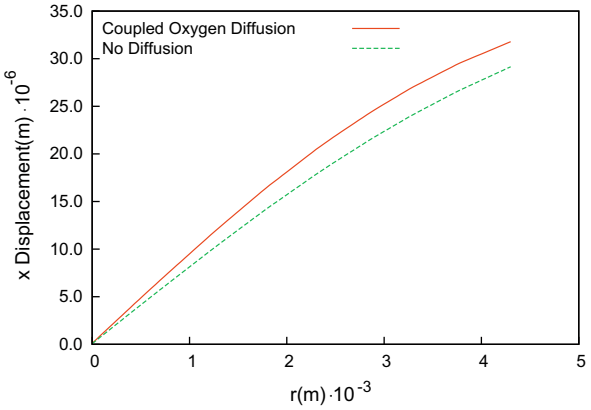

(b) Pellet x displacement as a function of radius, showing the impact of oxygen diffusion.

Fig. 4. Results of JFNK solution of coupled thermomechanics/oxygen diffusion system. Figure (a) shows pellet temperature as a function of radius from the pellet center which compares with the results of Ramirez [3] (but in 3D). Figure (b) shows the impact of coupled oxygen diffusion on thermal expansion as a function of radius from the center. Values are taken midway between the top and bottom of the pellet.

Fig. 5 shows the effectiveness of the JFNK solver. Note the strong reduction in nonlinear residual with increasing Newton iterations. In comparing the results with and without the oxygen diffusion equation; presence of the oxygen diffusion equation negatively impacts the nonlinear convergence somewhat.

3.2. Transient results

The next set of results considered were developed to compare with Fig. 6 in [3]. In this case, a Dirichlet condition for hyperstoichiometry $x = 0.01$ is applied on the outside of the pellet. The heat flux from the outside surface of the pellet is described by (2). In this equation, T_p is the instantaneous temperature on the outside of the pellet, $T_w = 750$ K, $L_g = 0.03$ mm, k(He) is from Table 1 using a temperature of $(T_p + T_w)/2$, $L_c = 0.5$ mm, and k(clad) is from Table 1 using a temperature of $0.1(T_p - T_w) + T_w$. In addition, initial conditions for hyperstoichiometry of $x = x_o = 0.01$ and temperature $T = T_o = 750$ K are applied across the pellet. The initial conditions for displacement correspond to the displacement field of a pellet at 750 K (note that zero displacement is defined to occur at $T_{\text{ref}} = 273$ K). The heat generation rate varies as a function of time,

$$\dot{Q}(t) = \dot{Q}_o + \frac{\dot{Q}_{\max} - \dot{Q}_o}{1 + 10\exp[-(-10 + t/\tau)]}, \tag{31}$$

where $\dot{Q}_o = 0\ \text{W m}^{-3}$, $\dot{Q}_{\max} = 2 \times 10^8\ \text{W m}^{-3}$, and $\tau = 45$ s.

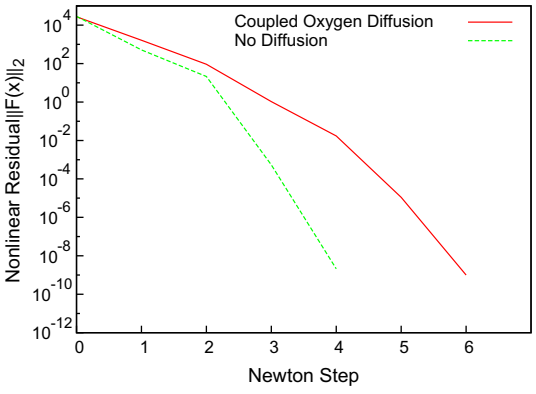

Fig. 5. Nonlinear convergence behavior of the JFNK solution of Eqs. (1)–(6). Note the strong convergence behavior of the nonlinear solver on the fully-coupled problem consisting of 2×10^5 unknowns. These results are preconditioned and are calculated in parallel.

Fig. 6 shows a plot of Lewis number $Le = \kappa/D$, for three different temperatures, $T = 800$ K, 1273 K, and 1400 K. The curves marked [3] are using the values of C_p and D from Ramirez et al. [3] (D_1 in Table 1), [12] uses the D from Higgs [12] (D_3 in Table 1), and [19] uses the D from Ruello [19] (D_2 in Table 1). When the C_p and D values given in Eqs. (1) and (2) of [3] are used to calculate Le, the results match Fig. 5 of that paper. These results are significantly different than Le calculated using data from other sources. As discussed in Table 1, the C_p given in Eq. (1) of [3] is roughly a factor of 1000 greater than those sources cited in Chapter 2 of [20]. Given this, this study assumed that the units in Eq. (1) of [3] are a typo and should be listed as $\text{m J kg}^{-1}\ \text{K}^{-1}$. If this is adjusted, Lewis numbers shown by the curves labeled as [3]* in Fig. 6 are obtained. The correlation proposed by [19] is given for $T = 1273$ K and is a function of x. The slope of this correlation matches [3]* up to $x = 3 \times 10^{-2}$, but is lower by a factor of 10. The correlation proposed by [12] does not account for x and thus does not match the slope of [3]* with increasing x. Further, this correlation is also lower by a factor of 2 for small values of x, and the curves separate further as x

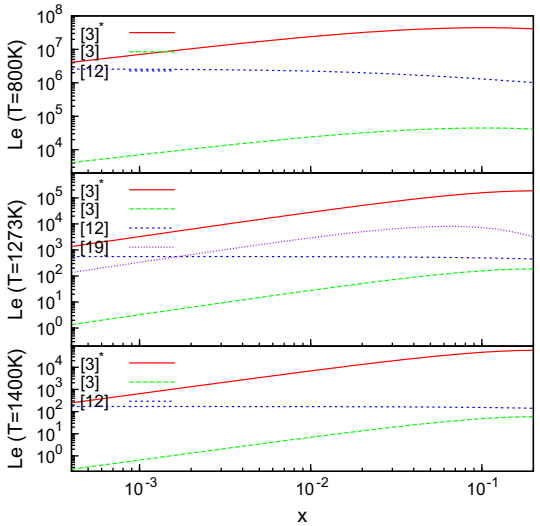

Fig. 6. Plot of the Lewis number $Le = \kappa/D$, where $\kappa = k/(\rho C_p)$ (all obtained from Table 1). Three sets of data for D are shown corresponding to D_1 obtained from [3], D_2 from Ruello et al. [19], and D_3 from Higgs et al. [12] (see text).

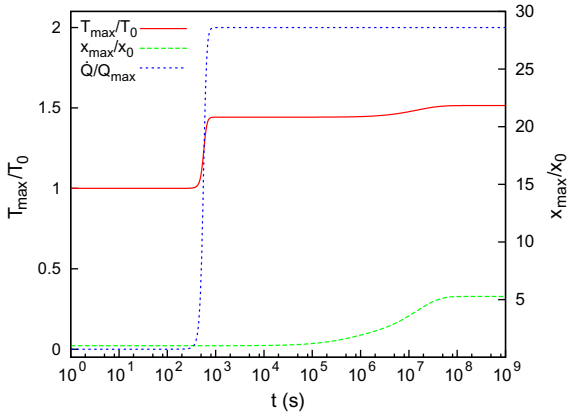

Fig. 7. Transient response for reactor start up from ambient conditions, using $\dot{Q}(t)$ given in the text, for comparison with Fig. 6 in [3]. In these results, $x_o = 0.01$.

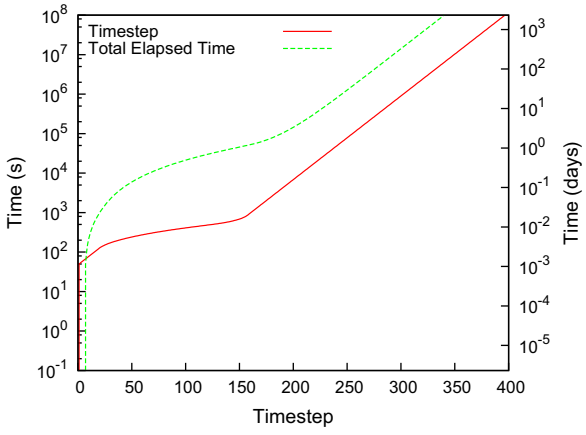

Fig. 8. Timestep history of the transient calculation.

increases. As the adjusted curves [3]* use D_1 which is a function of both temperature and hyperstoichiometry, this correlation was used in these results.

Fig. 7 shows the transient response of the three dimensional pellet given the above conditions. In this figure, only the results that correspond to $x_o = 0.01$ are shown, and $\dot{Q}$, x_o, and T_o are identical to those used to generate Fig. 6 of [3]. The results are very similar, with the exception of a 'steeper' response of T_{max}/T_o to the ramp in $\dot{Q}$, and a difference in time scales between the thermal and diffusion responses. As the data used in this transient correspond to the [3]* Lewis number curves in Fig. 6, these differences are likely due to the Lewis number issue discussed in the last paragraph.

These results employ a dynamical time step mechanism similar to that proposed in [30], and Fig. 8 shows the timestep history of this calculation. The solution methodology in BISON is fully-implicit; there is no need to limit the timestep to achieve numerical stability with this approach. This level of flexibility will be very important for extended burnup calculations, allowing long duration timesteps to be employed when the fuel properties and structure is changing slowly.

Lastly, Fig. 9 shows the transient displacement of the pellet with respect to time. Fig. 9(a) shows the radial displacement of the pellet at the outer edge, at a location on top of the pellet, and at a location 1/4 the way down. The displacement is clearly two dimensional, the top of the pellet expands outward further than the midsection. Towards the end of the simulation ($t > 1\times10^6$ s), oxygen diffusion impacts both the modulus and temperature to cause further pellet expansion in the radial direction. Similar behavior is seen in the axial displacement shown in Fig. 9(b).

3.3. Three dimensional results

The final topic of this report is a demonstration of parallel, three dimensional, fully-coupled thermomechanics of a simple, cracked pellet. Again, only the pellet is meshed, but the presence of the predefined crack in the mesh and the boundary conditions on the top and bottom of the pellet create a true three dimensional result, shown in Fig. 10. While this is an idealized example, it serves to illustrate the ability to perform true three dimensional parallel simulation within BISON on a more representative, dished pellet, geometry.

The parallel simulation was run on 512 processors of INL's Ice-Storm computer. The boundary conditions consisted of the pellet bottom resting on a frictionless surface. The initial condition was a constant heat generation term to mimic a constant energy generation rate within the pellet. Thermal heating of the pellet then ensues, directly leading to deformation of the pellet.

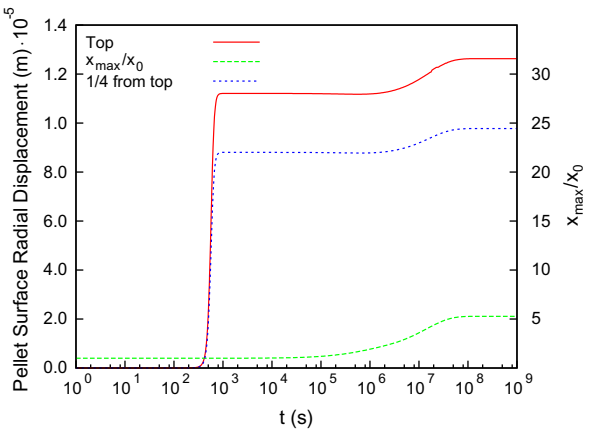

(a) Radial displacement of the pellet shown at the top of the pellet and at a point 1/4 down from the top. Note the impact of hyperstoichiometry on the radial displacement.

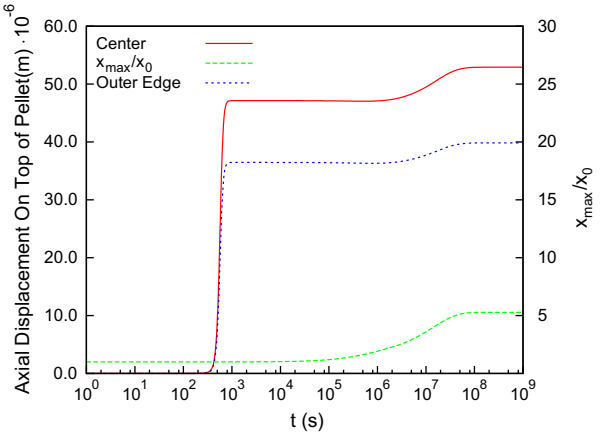

(b) Axial displacement of the pellet shown at the center of the pellet and at the outer edge.

Fig. 9. Displacement of the pellet at selected locations as a function of time and hyperstoichiometry.

Fig. 11(a) illustrates an exaggerated view, where the magnitude of displacement was increased by a factor of 10 to highlight the deformation local to the crack. The three dimensional behavior of the cracked pellet is apparent in this diagram, note the raised edge near the root of the crack on top of the pellet. This raised area quickly decays to the mean elevation of the dish a short distance away from the crack. Also note the deformation toward the cladding near the outer edge of the crack. It is clear, even with this simple model, that local deformation near cracks will significantly alter the geometry of the pellet in these areas and the mechanics of its interaction with the cladding. Fig. 11(b) depicts an oxygen diffusion simulation of similar, but uncracked, pellet geometry. The legend in the diagram corresponds to the degree of hyperstoichiometry x in the oxide.

4. Summary

This study develops a system of fully-coupled nonlinear, transient partial differential equations for a thermomechanics/oxygen diffusion problem that serve as a simple example of a UO_2 fuel pellet for comparison with one dimensional data by Ramirez et al. [3]. The MOOSE framework was employed to enable efficient solution of finite element discretizations via parallel JFNK methods [13]. With the exception of the Lewis number issue discussed in the previous

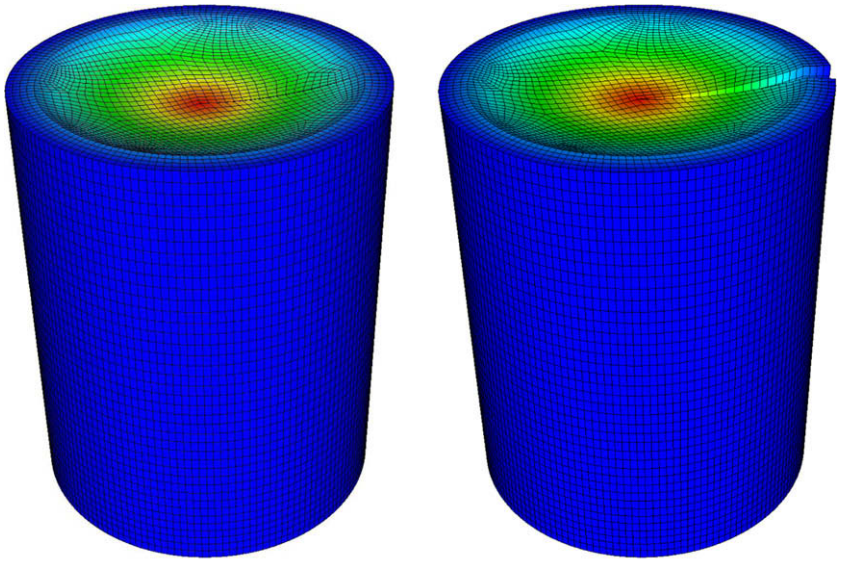

(a) Initial cracked pellet. **(b)** Cracked pellet in thermal equilibrium.

Fig. 10. Parallel three dimensional representative simulation of a dished pellet showing a crack extending from the center of the pellet to the right outer edge, where (a) shows pellet at the onset of thermal expansion and (b) shows pellet in thermal and mechanical equilibrium. Note how crack opens due to thermal expansion of the pellet.

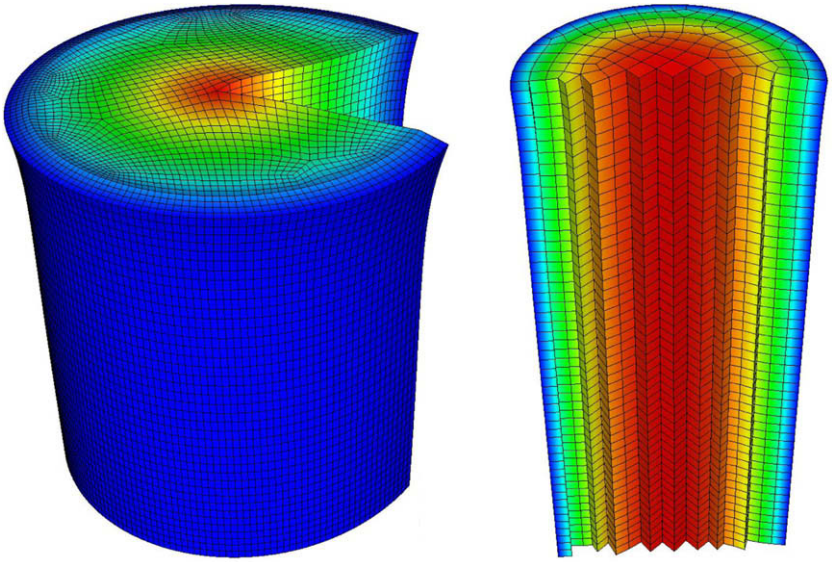

(a) Displacement magnified by factor of 10. **(b)** Degree of hyperstoichiometry in th pellet.

Fig. 11. Representative simulation of UO_2 pellet showing oxygen diffusion coupled to thermomechanics. Figure (a) shows the thermomechanical equilibrium results from Fig. 10 with the displacement magnified by a factor of 10 to illustrate complex deformation near the 'root' of the crack. In (b), the coloration indicates the degree of hyperstoichiometry (x) in the pellet, or $UO_{(2+x)}$.

section, this study presented results that were in general agreement with [3] for a steady state and transient pellet simulation.

In so doing, the proposed preconditioned JFNK approach demonstrated strong nonlinear convergence on a multiprocessor simulation of a pellet possessing 2×10^5 unknowns. To extend these results, a finer dished pellet simulation containing an idealized fracture demonstrated the capability of the code on a true three dimensional problem using a larger number of processors. While this report describes an initial framework that is physically incomplete, the demonstration of a robust implicit thermomechanical basis is certainly a requirement to be satisfied on the path to more comprehensive and representative fuel physics, and ultimately a useful fuel performance simulation capability.

In closing, the proposed approach as implemented in BISON appears quite effective for the three dimensional fuel pellet configurations examined, giving excellent nonlinear convergence properties on the combined system. Fully-coupled solutions of three dimensional thermomechanics coupled with oxygen diffusion appear quite plausible (and efficient) using the JFNK approach described here.

Acknowledgements

The submitted manuscript has been authored by a contractor of the U.S. Government under Contract No. DEAC07-05ID14517 (INL/JOU-08-15115). Accordingly, the U.S. Government retains a non-exclusive, royalty-free license to publish or reproduce the published form of this contribution, or allow others to do so, for U.S. Government purposes.

References

[1] Electric Power Research Institute, Frequently Asked Questions: Fuel Reliability Guidelines, <http://mydocs.epri.com/docs/public/FRP%20DEL%20FAQ1c.pdf>, 2008.
[2] J.C. Killeen, J.A. Turnbull, E. Sartori, in: Proceedings of the 2007 International LWR Fuel Performance Meeting, San Francisco, California, Paper 1102, 2007.
[3] J. Ramirez, M. Stan, P. Cristea, J. Nucl. Mater. 359 (3) (2006) 174.
[4] J.N. Shadid, R. Hooper, Trilinos Pellet Transport Example Code. <http://trilinos.sandia.gov>.
[5] D.L. Ropp, J.N. Shadid, C.C. Ober, J. Comput. Phys. 194 (2) (2004) 544.
[6] D.L. Ropp, J.N. Shadid, J. Comput. Phys. 203 (2) (2005) 449.
[7] V.A. Mousseau, J. Comput. Phys. 200 (2004) 104.
[8] D.A. Knoll, D.E. Keyes, J. Comput. Phys. 193 (2) (2004) 357.
[9] D.A. Knoll, V.A. Mousseau, L. Chacon, J.M. Reisner, SIAM J. Sci. Comput. 25 (2005) 213.
[10] J.M. Reisner, A. Wyszogrodzki, V.A. Mousseau, D.A. Knoll, J. Comput. Phys. 189 (2003) 30.
[11] V.A. Mousseau, D.A. Knoll, J. Comput. Phys. 190 (2003) 42.
[12] J.D. Higgs, B.J. Lewis, W.T. Thompson, Z. He, J. Nucl. Mater. 366 (2007) 99.
[13] D. Gaston, C. Newman, G. Hansen, D. Lebrun-Grandié, Nucl. Eng. Design, submitted for publication.
[14] D. Olander, Fundamental Aspects of Nuclear Reactor Fuel Elements, Technical Information Center, Energy Research and Development Administration, 1976.
[15] B. Michel, J. Sercombe, G. Thouvenin, Nucl. Eng. Design 238 (2008) 1612.
[16] D.G. Martin, J. Nucl. Mater. 152 (2) (1988) 94.
[17] J.K. Fink, Thermal Expansion of Solid Uranium Dioxide, <http://www.insc.anl.gov/matprop/uo2/thrm_exp/solid/expsuo2.pdf>, 1999.
[18] J.K. Fink, J. Nucl. Mater. 279 (1) (2000) 1.
[19] P. Ruello, G. Chirlesan, G. Petot-Ervas, C. Petot, L. Desgranges, J. Nucl. Mater. 325 (2004) 202.
[20] J.K. Hohorst, SCDAP/RELAP5/MOD2 Code Manual, Volume. 4: MATPRO–A Library of Materials Properties for Light-Water-Reactor Accident Analysis, Technical Report, NUREG/CR-5273, EGG-2555, 1990.
[21] U.M. Ascher, L.R. Petzold, Computer Methods for Ordinary Differential Equations and Differential–Algebraic Equations, SIAM, Philadelphia, PA, 1998.
[22] Y. Saad, Iterative Methods for Sparse Linear Systems, The PWS Series in Computer Science, PWS Publishing Company, Boston, MA, 1995.
[23] M. Pernice, H.F. Walker, SIAM J. Sci. Comput. 19 (1) (1998) 302.
[24] D.A. Knoll, W.J. Rider, SIAM J. Sci. Comput. 21 (2000) 691.
[25] L. Chacon, D.A. Knoll, J.M. Finn, J. Comput. Phys. 178 (2002) 15.
[26] V.E. Henson, U.M. Yang, Appl. Numer. Math. 41 (2000) 155.
[27] R.D. Falgout, U.M. Yang, in: International Conference on Computational Science, vol. 3, 2002, p. 632.
[28] Satish Balay, Kris Buschelman, Victor Eijkhout, William D. Gropp, Dinesh Kaushik, Matthew G. Knepley, Lois Curfman McInnes, Barry F. Smith, Hong Zhang, PETSc Users Manual, Technical Report ANL-95/11 – Revision 2.1.5, Argonne National Laboratory, 2004.
[29] Sandia National Laboratories, CUBIT: Geometry and Mesh Generation Toolkit, <http://cubit.sandia.gov>, 2008.
[30] M.A. Pope, V.A. Mousseau, in: The 12th International Topical Meeting on Nuclear Reactor Thermal Hydraulics (NURETH-12), Log Number: 239, Sheraton Station Square, Pittsburgh, Pennsylvania, USA., 2007.